

High-Resolution Four-dimensional Surface Reconstruction of the Right Heart and Pulmonary Arteries

Peter J. Yim^{1*}, Desok Kim², Carol Lucas¹

¹Department of Biomedical Engineering, ²Department of Surgery
University of North Carolina, Chapel Hill, NC 27599

ABSTRACT

Determination of the surface of the heart is a challenging problem due to the heart's motion and the potential importance of subtle geometric features. The Meyer watershed has been shown to be an effective solution to this problem in images of the left ventricle in at least two medical image types. In this paper the technique is extended, first of all, by application to the right ventricle (RV) in images from the Dynamic Spatial Reconstructor (DSR). Additionally, several important issues related to its general application are addressed including (a) image anisotropy (b) four-dimensional processing and (c) valve localization. The Meyer watershed model itself is also discussed in some detail with respect to its implementation and general properties. A simple by-product of surface reconstruction of the RV in the DSR images is that of the pulmonary arteries.

Typically, different mechanisms are responsible for the acquisition of each dimension of a multidimensional image and thus the true resolution of the image may differ in any or all directions. Such is the case in the DSR images although anisotropy is substantially moderated by modification of the slice thickness, acquisition time and in-plane pixel size. The anisotropy of these images was thus studied empirically with edge-tracking studies. In these studies, directional components of the sobel edge were independently varied so as to optimize the edge-tracking in the inter-slice direction and in the inter-frame direction. From these studies, the inter-frame edges are found to be the strongest and estimated to be 2.4 times greater than the in-plane edges while the inter-plane edges are the weakest and estimated to be 0.6 times the in-plane edges. An optimal anisotropic sobel filter was designed accordingly.

Four-dimensional processing of the images, at all steps, is a straight-forward extension from 2D and 3D processing except that the final 4D surface must be transformed to 3D, for visualization *etc.* Thus, a de-blurring operation is defined, whereby a 3D Meyer watershed is performed on the sobel image restricted to the 4D surface. This operation primarily effects regions where large inter-frame motion occurs. One benefit of the 4D processing is a nearly absolute minimization of user interaction; in this case, a image of 16 frames of 100 slices each was reconstructed with gross operator definition of ventricular interior and exterior on a single slice plus two other minor markings to enhance the definition of the anatomically important tricuspid region.

For the clinically and physiologically important volume calculation, techniques are needed for accurate determination of the valve locations. Landmarks on the RV in both systole and diastole were found for location of the tricuspid and pulmonary valves from which planes could be generated for occlusion of the RV chamber. Ejection fraction in a single canine RV was found to be 0.57. Comparison of short-axis cross-sections shows marked differences between contraction in the inflow and outflow regions.

1. Introduction

Quantification of ventricular shape and size from medical images has been an important goal of cardiology from its inception. Thus numerous geometric and surface models have been proposed for calculating volume and extracting, in the most systematic and reliable manner, the boundaries of the heart in the images, and in particular the boundaries of the ventricular chamber^{5,15,18-23}.

* All correspondence to pyim@bme.unc.edu

One technique, first proposed by F. Meyer³ (and henceforth to be referred to as the Meyer watershed) has had exceptional success in ventricular surface reconstruction in two separate reports; in one of a 3D time series of a nuclear medicine image⁶ and in the other of the 3D portion of the Dynamic Spatial Reconstructor (DSR) image⁵. . In both cases user interaction was found to be minimal with the surface reconstruction relatively insensitive to variation in user interaction. The work to be presented here represents first the extension of this technique to the fourth (temporal) dimension with suggestions for handling the effects of anisotropy which are compounded with each higher dimension. Incidentally, an important new conceptualization of both the general watershed segmentation and the Meyer watershed was developed and is presented here in some detail.

This work also represents the first application of this technique to images of the RV of the DSR, which due to both the high spatial and temporal resolution is uniquely suited for the scientific study of the heart mechanics. Based on 2 and 3D visualizations a number of mechanically relevant features are presented from the single heart analyzed to date.

2. Background: The watershed approach

The watershed segmentation approach found wide use in medical image processing¹⁻⁶ in addition to other areas including metallurgy⁷ and road traffic sensing³. This segmentation technique is derived directly from the topographical watershed concept whereby all points on the surface are classified according to drainage, *i.e.* any two points are in the same region (catchment basin) if they drain to the same point. Thus, the watershed effectively subdivides the image as shown in figure 1. At the smallest or most fundamental level, the set of drainage destinations on a terrain or in the intensity surface of an image are all the local minima. The watershed lines which divide the regions constitute a set of edges which are valid at both the local and more global levels; *i.e.* no smoothing constraints are imposed on the local edges and all edges are entirely continuous.

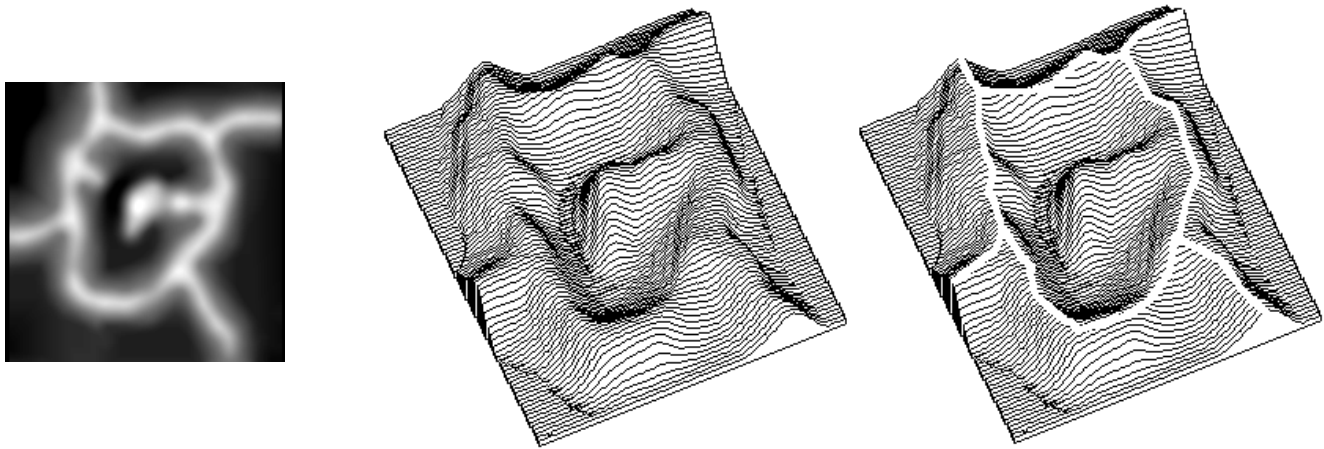


Figure 1. The watershed analogy. A gradient image (left) is viewed as a topographical relief whose elevation at any point is the image pixel intensity (center). All points which drain to a common point (local minimum) form a local watershed region (catchment basin) and the borders between the regions are the watershed lines as shown in white outline. (right)

The direct drainage analogy does in some cases produce ambiguous regions and an immersion analogy, which is otherwise equivalent, is preferred. In this analogy, the surface is immersed in water, with water emerging from each local minima. At each point where water from different local minima meet, a dam is formed with the process continuing until all minima are fully surrounded by dams which are the watershed lines.

In practice, meaningful objects in an image are rarely segmented correctly by the basic watershed. Rather, the watershed tends to oversegment the image. A number of strategies have thus been devised for revising the initial segmentation of the watershed to produce fewer, more meaningful regions. These include application-specific criteria for grouping adjacent regions^{3,7} and more general approaches such as the multi-resolution approach of Gauch and Pizer⁸. For cardiac images where complete automation is not a priority, the proposal of F. Meyer has been preferred. In this technique, the analogy is equivalent to that of the basic or local watershed except that the water emerges only from the points specified by the user referred to as markers. This technique

is illustrated in figure 2. In the case of the cardiac image, those points or regions would be the gross designations of the interior and exterior of the cardiac chamber.

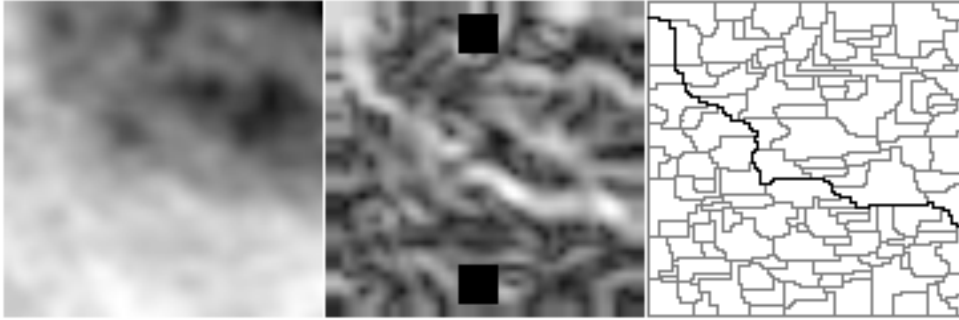


Figure 2. The Meyer watershed. Markers (black squares in this case) placed on a gradient image (center) propagate throughout the gradient image through flooding so as to produce a single line of separation (right) which is quite plausible in visual comparison with the original image (left). As will be shown below, the Meyer watershed line is composed of segments from the original web of watershed lines. (This figure is illustrative in nature; the Meyer watershed was formed from 32K-grey-level, 4-neighbour flooding algorithm which must be manually matched, due to small-scale difference, to a local watershed formed from a 256 gray level, 8-neighbour algorithm.)

3 A pathwise formulation of the watershed and implications

3.1 The pathwise formulation

It is generally understood that the watershed lines follow the ridges in the intensity surface and avoid the valleys. Such a definition, which also applies in its essentials to the Meyer watershed with a generalization of terms, provides a good basis for understanding the Meyer watershed and comparison with other boundary-formation techniques.

Generally, even with the immersion analogy of the watershed, potential ambiguity in the location of the watershed still exists due to plateaus or other situations where two pixels in the image share the same value. A simple solution to this problem, and conceptually as valid as any other, is to expand the intensity range and mildly blur the image so that no two pixels in the image have the same value as suggested by Gauss and Pizer. In practice this assumption can be approximated to any degree desired. The discussion to follow will incorporate this assumption for the purposes of simplicity.

The following property, to be referred to as the pathwise criterion, applies to both the local and the Meyer watershed, when the term “watershed minima” are true local minima for the local watershed and are the imposed markers for the Meyer watershed.

Theorem 1. *A watershed line is a path surrounding one and only one “watershed minima” for which, between any two points on the watershed path a and b the watershed path between (not including) a and b has a minimum greater than or equal to that of any alternate, homotopic⁹ (no watershed minima between the watershed and the alternate paths) path.*

$$\forall A_i(a,b), \text{Min}(W(a,b)) \geq \text{Min}(A_i(a,b)) \quad (1)$$

In other words: **A segment of a watershed boundary is only as strong as it's weakest point.**

$I(x)$ is intensity value or height at point x .

And where a path is a set of contiguous pixels:

$W(x,y)$ is a continuous watershed path from x to y generated by the immersion procedure; $x,y \notin W(x,y)$

$A_i(x,y)$ is some continuous, alternate, homotopic path from x to y ; $x,y \notin A_i(x,y)$

$D(x,y)$ is a continuous drainage path from x to y , $x,y \notin D(x,y)$, such that $\forall x \in D(x,y), I(z) < I(x)$

$R1, R2, R3$ are three watershed regions.

$\text{Min}(P)$ is the point in the set P with the minimum intensity value.

By the immersion analogy, from each point on a watershed path $W(a,b)$ there exists a drainage path to at least two different regional minimum, as shown by the dotted line in figure 3.

$$\forall x \in W(a,b), \exists D(x, \text{Min}(R_1)), D(x, \text{Min}(R_2)) \quad (2)$$

and by the definition of the drainage path:

$$\forall y \in D(\text{Min}(W(a,b)), \text{Min}(R_i)), I(y) < I(\text{Min}(W(a,b))). \quad (3)$$

A complete path connecting the minima of those two adjacent regions, $\text{Min}(R_1)$ and $\text{Min}(R_2)$, can be formed from the from the two drainage paths defined as :

$$D_{\text{tot}} \equiv D(\text{Min}(W(a,b)), \text{Min}(R_1)) \dot{\cup} D(\text{Min}(W(a,b)), \text{Min}(R_2)) \dot{\cup} \text{Min}(W(a,b)) \quad (4)$$

whose minimum must thus be less than or equal to the watershed line minimum, $\text{Min}(W(a,b))$

$$\text{Min}(D_{\text{tot}}) \leq \text{Max}(D_{\text{tot}}) = \text{Min}(W(a,b)) \quad (5)$$

Any alternate, homotopic path between a and b must contain at least one point x in D_{tot} .

$$\forall A_i(a,b), \exists x \in A_i(a,b) \cap D_{\text{tot}} \quad (6)$$

$$\text{Min}(A_i(a,b)) \leq I(x) \leq \text{Min}(W(a,b)) \quad (7)$$

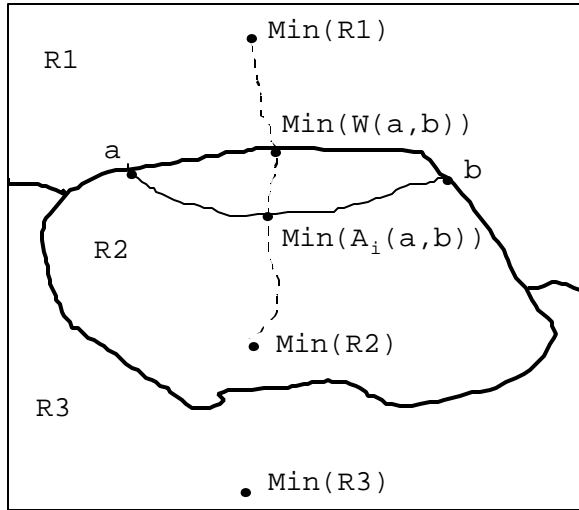


Figure 3. The pathwise criterion of the watershed. All watershed paths satisfy pathwise criterion. Symbols and functions defined in text. Dark lines are watershed lines, thin line is alternate, homotopic path, and dotted lines are drainage paths.

Theorem 2.. In the case the watershed minima are the local minima, the watershed lines are the only paths which satisfy the pathwise criterion.

There are three possible contrary cases that have to be considered.

case 1: There is an alternate, homotopic path which satisfies the pathwise definition which does not intersect with any watershed line, i.e. it is entirely within a single watershed region.

case 2: There is an alternate, homotopic path which satisfies the pathwise definition which intersects a watershed path only once.

case 3: There is an alternate, homotopic path which satisfies the pathwise definition which has two or more intersections with the watershed path.

Case 3 will be discussed first. In this case, the alternate path between any two consecutive intersections, a and b in figure 3, must be entirely within one watershed region, say R_2 . The alternative path $A_i(a,b)$ must contain a point in $D(\text{Min}(W(a,b)), \text{Min}(R_2))$.

$$\forall A_i(a,b) \exists x \in A_i(a,b) \cap D(\text{Min}(W(a,b)), \text{Min}(R_2)). \quad (8)$$

and therefore

$$\text{Min}(A_i(a,b)) \leq \text{Min}(D(\text{Min}(W(a,b)), \text{Min}(R_2))) < \text{Min}(W(a,b)) \quad (9)$$

in contradiction to the pathwise criterion.

Case 1 will be discussed next. As shown in figure 4:

“Water” is the watershed line surrounding a single local minima,

“Conc” is some alternate path surrounding that same local minima and entirely within Water.

R_{ext} is the region between Water and Conc, including the points on Water, R_{int} is the region within Conc.

“c” is any point in R_{ext} and “d” is some point on Conc.

M is the local minima

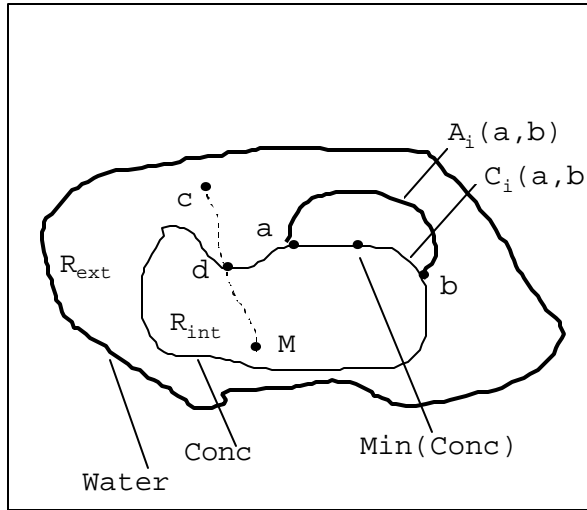


Figure 4. The pathwise formulation of the watershed is unique to the watershed path. Any alternate, path concentric (Conc) with the watershed path (Water) cannot be superior, by the pathwise formulation, to all alternative paths (A_i). Other labels defined in text..

By the definition of the watershed based on the local minima, all points in the watershed region, all points must be able to drain to the local minima. In other words:

$$\exists D(c, M) \forall c \in R_{\text{ext}} \quad (10)$$

This implies that for all points in the region R_{ext} there is at least one point on Conc which is lower:

$$\forall c \in R_{\text{ext}}, \exists d \in \text{Conc} \text{ such that } I(c) > I(d) \quad (11)$$

Thus:

$$\forall c \in R_{\text{ext}}, I(c) > I(\text{Min}(\text{Conc})) \quad (12)$$

It is then clear that any alternative, homotopic path $A_i(a,b)$ which is in R_{ext} which does not include $\text{Min}(\text{Conc})$ must be superior by the pathwise criterion to the segment of the concentric path $C_i(a,b)$.

Case 2 is only trivially different from case 3 since the alternate path is entirely within the single local watershed except for the point(s) at the single intersection. In this case it can be shown that all points in the R_{ext} are greater than $\text{Min}(\text{Conc})$ (not including the points at the intersection) and thus the same contradictory path can be constructed.

Theorem 3. The pathwise property does not, however, uniquely satisfied by the Meyer watershed path.

In the case of multiple concentric ridges surrounding the marker, each separated by low valleys: each concentric ridge might satisfy the greater-minima criterion while only the ridge with the greatest minima would be the Meyer watershed line.

Theorem 4. The Meyer watershed is composed entirely of segments of the “local” watershed lines (where watershed minima refers to local minima) of the marked image (all points in the markers are considered as being part of local minima).

The three possible contrary cases are exactly the same as for theorem 2; the Meyer watershed intersects two or more times, once, or not at all with the web of “local” watershed lines. Thus the proof is the same.

Theorem 5. The “local” watershed lines of the marked image are the same as those of the original image except in an original local watershed region penetrated by a marker (the marker includes a point in the watershed line surrounding the region).

Imposition of markers on the image (creation of local minima) will only eliminate potential alternative paths between any two points. Thus, unless a local watershed line is broken by the imposition of the markers, the watershed path, as it exists in the original image, will remain superior to all other paths, as required by the pathwise criterion.

3.2 Comparison of Meyer watershed with active contour approach

The pathwise formulation of the Meyer watershed allows for a direct comparison with the active contour approach in which the boundary is explicitly derived from a pathwise properties¹⁴. In general, the active contour favors the path along a set of points with the greatest average pixel intensity with penalties for spatial and shape discontinuity. In contrast, the watershed, and its global counterpart, the Meyer watershed are sensitive only to the lowest pixel intensity in a given path. Edges which are sufficiently isolated, no matter how strong in intensity, will be rejected in the formation of the Meyer watershed while likely to be accepted, if of sufficient strength, in the active contour.

The active contour approach has been applied in numerous cases to cardiac ventricular surface reconstruction, particularly with cardiac ultrasound¹⁵ but is less attractive for this application where ventricular shape itself is of particular interest and that shape is known to be highly diverse. Under those circumstances, the smoothing properties of the active contour¹⁴, which are essential to it for the reconciliation of local and global shape, are likely to produce undesirable bias in the results. In contrast, in the watershed approach there is no such bias or requirements of local shape assumptions.

4. Application

4.1 The DSR image of the RV

Briefly, the images of the RV were acquired with the Dynamic Spatial Reconstructor in the transverse imaging plane with isotropic voxel dimensions of 0.8 mm (0.9 mm for the image from which the pulmonary arteries, (PA) were reconstructed) (Basic technique described in Jorgensen et al¹³). 16 contiguous time frames are acquired of 33msec in duration. The right atrium (RA), RV, and PA are opacified in the first pass of the contrast agent inject as a bolus into the superior vena cava. Image edge strength is greatest in the RA and PA where there is an almost direct transition from the high intensity blood to the low intensity extra-cardiac tissue. Both the endo- and the epicardial surfaces (interior and exterior) of the RV freewall are visible but, especially at end-diastole when it is thinnest, are potentially confused due to noise and streaking in the image. Opacification of the RA is quite variable regionally and through time and thus reconstruction of its entire surface has not been possible.

4.2 Extension of the Meyer watershed to multidimensional images

The most useful property of the DSR heart image data set is not only the high spatial and temporal resolution of the images but also the approximate isotropy of the image in all those directions, which allows for the extension of 2D techniques into 3 and

4D. Visually, the topographical model of the watershed is no longer useful at the higher dimensions, but conceptually all the algorithms and principles are the same. In 3D, the watershed boundary is a surface. The pathwise formulation of the watershed applies equally well to the higher dimensions with minor redefinition of terms. For example, in 3D, it is the *surface patch* with the greatest minima which closes any given opening in the boundary surface, which must be the watershed boundary. Generally, processing of the images in 3 or 4D both improves the accuracy of the boundary formation by increasing the information by which the border at any given point is determined and reduces the operator role in the processing. Specifically, markers can be placed on fewer slices and perhaps more importantly, in slices where the boundary is most poorly defined due to the angle of the slice plane, marker information need not be supplied. Higgins and Ojard⁵ developed and applied the 3D Meyer watershed for the LV in the DSR image.

Similar advantages can also be obtained by the extension of the processing to the temporal dimension. Particularly in regions where the boundary is ambiguous due to motion, consultation with the border in that region in nearby time frames may be helpful. This is important for the reliable study of the time course of mechanical events from the images. Again, the watershed principle, while no longer visualizable in terms of drainage on an intensity surface, extends directly to the fourth dimension. Friedlander⁶ applied the 3D Meyer watershed to a time-series of a single slice in a cardiac nuclear medicine image with high reproducibility. The work to be presented here represents, to our best knowledge, the first application of the watershed principle to 4D.

4.3 Empirical assessment and compensation for image anisotropy

A high degree of freedom exists in the reconstruction of the DSR 4D image for optimization of the resolution due to the very fine fundamental slice-thickness and acquisition time-window size from which integer multiples can be generated *a posteriori*. In order to simplify interpretation and processing of the images, the stated goal of the image reconstruction was to equalize the resolution in all directions. However, production of an entirely isotropic 4D image, *ie* matching of the in-plane, inter-slice, and inter-frame resolutions, is only approximate and likely to vary with the imaging conditions¹¹. A method was thus devised for assessing and compensating for any remaining anisotropy in the images.

The method of assessment involves the multidimensional Meyer watershed itself, which is appropriate since it is dependent on isotropy of the image, without which errors in the surface reconstruction can be produced at both the local and global levels. The general procedure is thus to reconstruct the surface using the Meyer watershed on the edge image after compensation for various hypothetical degrees of anisotropy. Presumably then, where the compensation is most accurate, the reconstructed surface will be the best.

Anisotropy can be reduced or compensated for by introducing independent scaling of each directional component into the sobel edge filter as in (10).

$$S = \sqrt{\alpha D_x^2 + \beta D_y^2 + \gamma D_z^2 + \lambda D_t^2} \quad (13)$$

where S is the sobel edge strength, D_x, D_y, D_z, D_t are the directional components (intensity change) of the sobel filter in the x,y,z, and t directions respectively, and $\alpha, \beta, \gamma, \lambda$ are the anisotropic scale factors in the x,y,z, and t directions respectively

The next question is then how to determine the “best” of the resulting surfaces and thus the optimal degree of compensation. Two similar objective criteria were developed based on the concept of propagation of the surface as described above. In this analysis each of the two independent potential anisotropies (inter-slice-to-in-plane and inter-frame-to-in-plane) were assessed independently by considering only either a single frame or a single slice in a time series image. The first criterion is to compare the surfaces generated from conservative estimates (by marker placement) of the surface location on two widely separated slices. The principle is that the surface is guaranteed to be sensible at the marked slice and most likely to be sensible at distant slices when the image is most isotropic. Thus the surfaces generated from the two widely separated slices will tend to diverge from one another when the image is more anisotropic and tend to agree with one another when the image is more isotropic. This technique is employed in the study of the inter-slice-to-in-plane anisotropy. Agreement between surfaces is quantified as the percent overlap of the two volumes within the 3D surfaces to the total volume within both surfaces. The results of this analysis are shown in figure 5. The optimal compensation is thus estimated to be $\gamma = 0.6$.

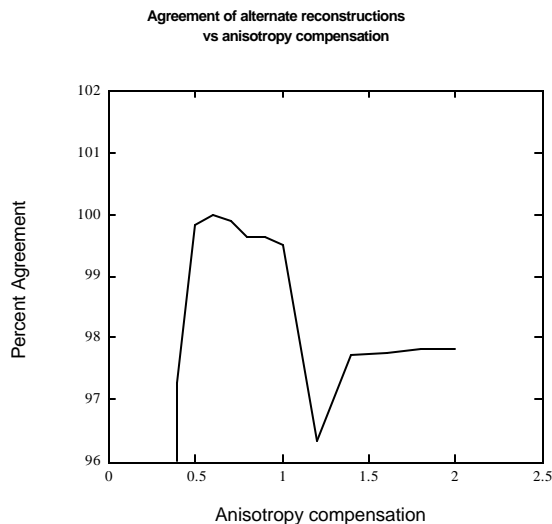


Figure 5. *Inter-slice-to-in-plane anisotropy. Best agreement between surface reconstruction based on markers placed on widely spaced markers in a single diastolic frame is achieved when the in-plane resolution is scaled by less than 1 (maximum agreement is at 0.6).*

The same technique could be employed in the study of the inter-frame-to-in-plane anisotropy but a modified version was found to more definitive due to the nature of the errors likely to occur and the limited temporal dimension relative to the in-plane dimensions. In the reconstruction of the surface of the RV, one obvious error likely to occur, particularly over the course of the contraction cycle within a single slice, is mistaking of the stronger epicardial edge for the desired endocardial edge due to the thinness of the freewall of the RV. In contrast, it is more difficult to visually estimate the true location of the septal surface of the chamber and the errors in this region are less definitive. Thus, it is probably most exact to judge the quality of the propagation in the temporal direction simply on whether the reconstructed surface adheres to the endocardial surface disregarding any other more subtle potential errors. A time series surface was thus judged to be either correct or incorrect based on the adherence to the endocardial border in a single slice distant from the markers. Since errors did not occur with regularity in the propagation of entire slices through the limited number of time frames (maximum of 14), various-sized sub-regions of the slices were selected so as amplify the importance of the propagation effect. These sub-regions ranged in size from 30 to 80 pixels wide. The results are shown in figure 6. Thus, the best inter-frame-to-in-plane compensation was estimated to be $\lambda=2.4$.

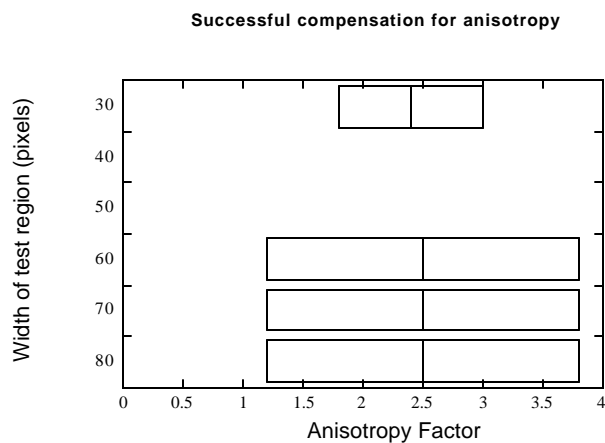


Figure 6. *Inter-frame-to-in-plane anisotropy. Anisotropy factor 1 estimated to be 2.4.*

4.4 De-blurring

Just as a digital 3D surface can have thickness or be “blurred” in any cross-section whenever it is sufficiently oblique to the plane of the cross-section, so too the 4D surface may be blurred in its occurrence in the 3D cross section where true motion occurs. While the blurring itself may contain useful information it is often necessary to have a single unambiguous surface at any time point. This can be produced by applying the 3D Meyer watershed to each frame of the 4D surface produced by the 4D Meyer watershed.

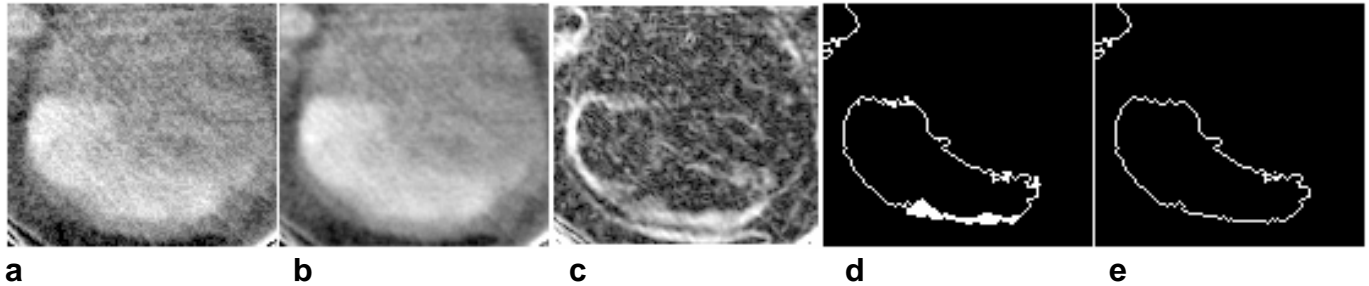


Figure 7. Processing of 4D DSR-RV image. Original image (a), 4D gaussian smoothed, space constant of 0.5 pixels (b), 4D anisotropic sobel filtered (c), segmented with the 4D Meyer watershed (d), and finally deblurred to 3D surface (e). Slice shown is in ejection phase with noticeable motion in anterior freewall (lower right in d).

Other than the final deblurring step, processing of the image is entirely four-dimensional in nature with no explicitly distinction of the temporal dimension of the image. The final processing of the image consisted of the following steps as shown in figure 7: 1. Light smoothing of the image with a 4D gaussian with space constant of 0.5 pixels. 2. Anisotropic sobel edge filtering with the relative amplification of the inter-slice edges by $1/0.6$ and attenuation of the inter-frame edge strengths by $1/(2.4)$. 3. Meyer watershed with ventricle defined with markers in a single diastolic slice and the tricuspid valve defined with minor markings in two other diastolic slices. The watershed flooding is based on 8-neighbour (4D) implementation. 4. Deblurring.

5. Preliminary observations of dynamic RV dynamic anatomy:

The ventricle is not a closed surface having substantial openings at both the inflow and outflow points, the tricuspid and pulmonary valves respectively. Particularly for the measurement of ventricular volume which is physiologically and clinically important, localization, or at least approximation of the ventricular boundary, at these points is necessary. Little difficulty is encountered in defining the pulmonary valve boundary since, first of all, it has relatively little motion over the cardiac cycle and secondly, since the ventricle has narrowed to a channel at that point, its exact location is relatively unimportant. On the other hand, the tricuspid valve experiences dramatic motion over the cardiac cycle and borders a wide region of the ventricle. In both cases, however, the DSR images provide sufficient chamber-tissue, and tissue-extra-cardiac resolution to locate the valves at various points. Generally, the valve locations are defined at end-diastole by a fairly sharp thinning of the tissue from the ventricle to the atrium or the pulmonary artery. In contrast, at end-systole, well defined discontinuities exist at the valves as the blood's shape flares out from the contracted ventricle. In the 3D visualizations, the surface of the ventricle at end systole is noticeably rougher in the ventricle than the atrium, probably due to greater trabeculation or inherent surface roughness and to the weaker chamber-tissue boundary of the ventricle versus chamber-extra-cardiac boundary of the atrium which produces greater random fluctuations in the boundary.

An end-diastolic and end-systolic frame of the right heart are shown in figure 8. A number of features of the ventricle are clearly visible in the reconstructed surface of the right heart. The atrium, in which the contrast is greatest since little tissue intervenes between the chamber and the air-filled lung tissue, properly appear with their smooth outer surface and relatively sharp corners toward the interior surface. Similarly, in the right ventricle, the valve regions are well defined as the constrictions of the chamber at the inflow and outflow. Ambiguity in the inflow region of the right ventricle, just below the tricuspid valve, was resolved with minimal operator assistance.

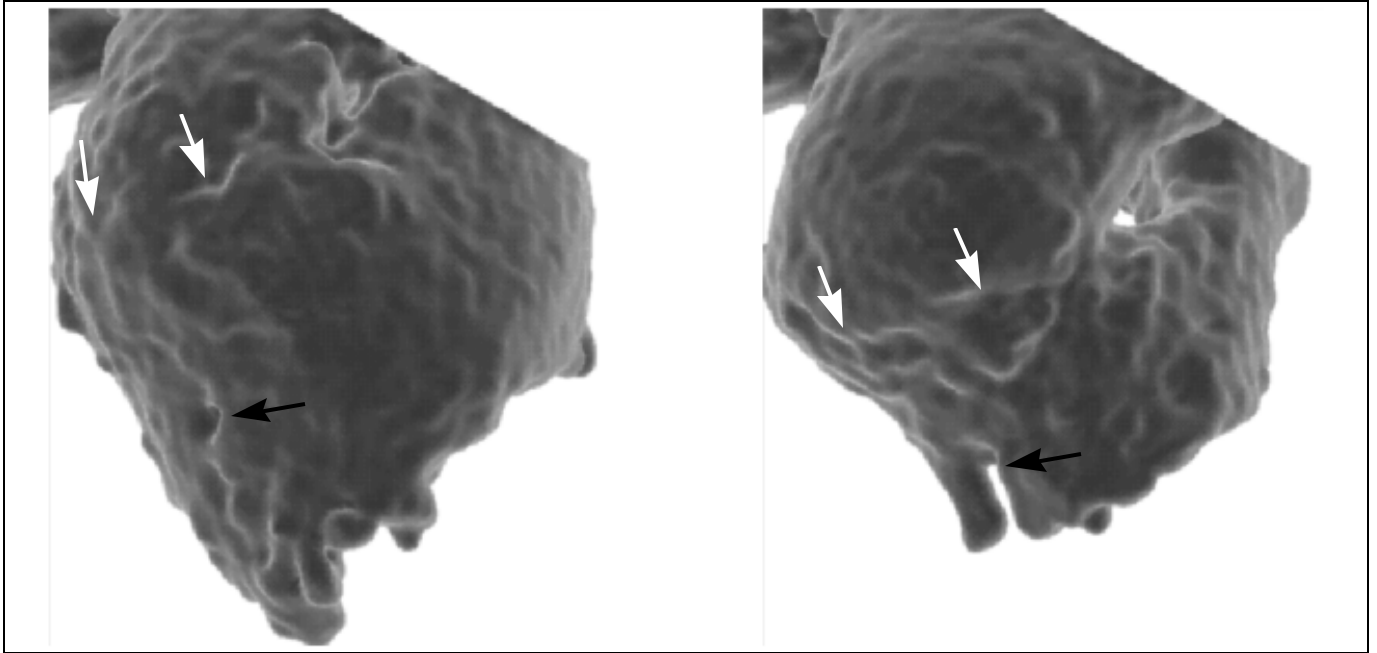


Figure 8. Visualization of end-diastolic (left) and end-systolic (right) frames of 4D reconstructed surface. White arrows indicate location of tricuspid valve and black arrow indicates band of muscle.

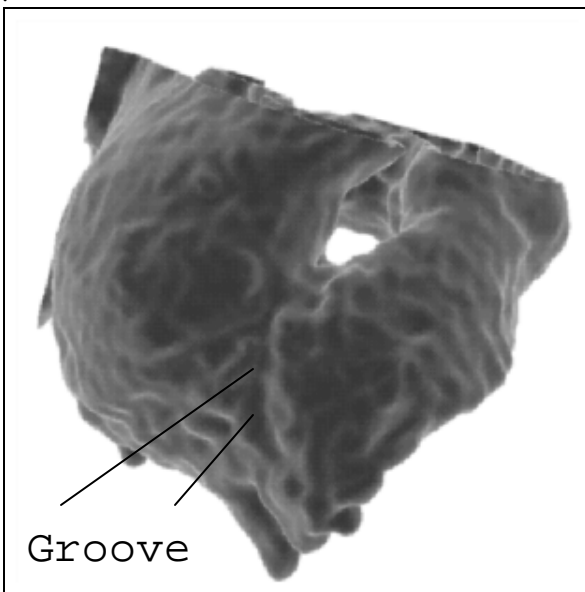


Figure 9. (left) Second view of end-systole. Groove between inflow and outflow region clearly visible.

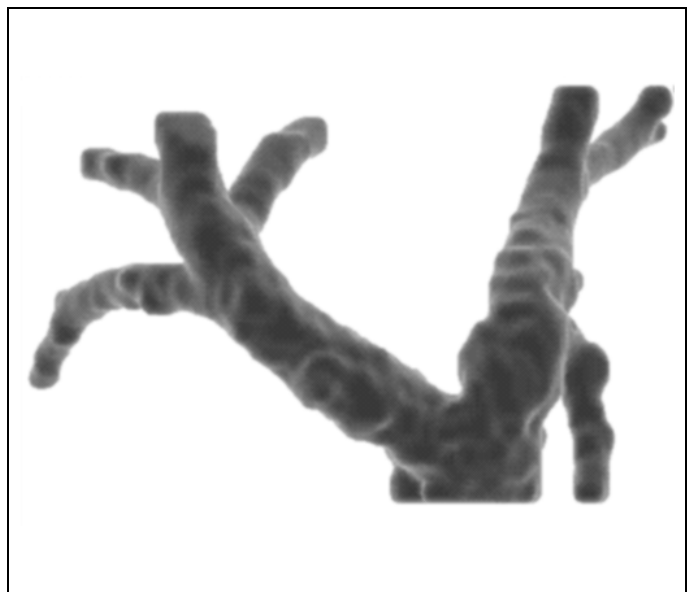


Figure 10.(right) Visualization of pulmonary artery tree reconstructed in 3D without compensation for anisotropy

Once the RV surface has been satisfactorily reconstructed, the RV can be studied in conventional anatomical methods. To begin with, the ejection fraction was found to be 0.57 (21.5 cc at end-systole, 49.5 cc at end-diastole) in the single canine heart thus studied with the volume at end-diastole and end-systole calculated according to:

$$\text{Volume} = \text{Chamber Interior Volume} + \frac{1}{2} \text{Chamber Boundary Volume} \quad (14)$$

The shapes of the RV at those two phases is shown in 3D in figure 8 and 9. Prominent in these views is (1) the substantial downwards movement of the tricuspid valve during the contraction (2) increased irregularity in the ventricular surface at end-diastole, which must be due to greater separation of the trabecular fibers from the main mass of the freewall. (3) particularly in figure 9, the appearance in systole of a sharp groove tending to separate the inflow region, or that closest to the tricuspid valve, from the outflow region, or that closest to the PA valve.

Short-axis slices at equivalent absolute locations from end-diastole and end-systole are superimposed in figure 11 which correspond in end-systole to directly below the tricuspid valve. In this specific 2D analysis, certainly no gross offset of the cross-sections due to twisting is observed although further analysis may show the presence of more subtle twisting which is known to play a very large role in LV contraction¹². However, there is clearly an asymmetry in the contraction whereby, in the short-axis view the outflow region undergoes a far greater contraction. In general terms, contraction of the RV can be characterized as follows: the inflow region contracts by a downwards sweeping motion of the tricuspid valve while a significant component of the outflow region's contraction is in the plane of the tricuspid valve and thus nearly perpendicular to contraction in the inflow region.

Reconstruction of the pulmonary arteries can be obtained from the same image set using essentially the same procedures as for the RV and can even conceivably be performed simultaneously with that of the RV. However, since the primary attention was the RV, in general the pulmonary arteries were neglected and due to computer memory limitations, good portions of the pulmonary arteries were cropped from the image. However, at an early stage in the development of reconstruction procedure, the PA was independently reconstructed in a second heart as shown in figure 10 (the image of this heart was truncated at the apex of the RV and as the RV reconstruction has not been presented). In this reconstruction, the heart image was first resliced as short-axis slices by rotations of 45 and 15 degrees about the x and y axis in sequence. The reconstruction was then performed in 3D with no compensation for anisotropy. In general, the edges of the pulmonary artery tend to be strong due to both the immediate step in intensity from the blood pool to the very low intensity extra-cardiac tissue and to the relative lack of motion in the pulmonary arteries.

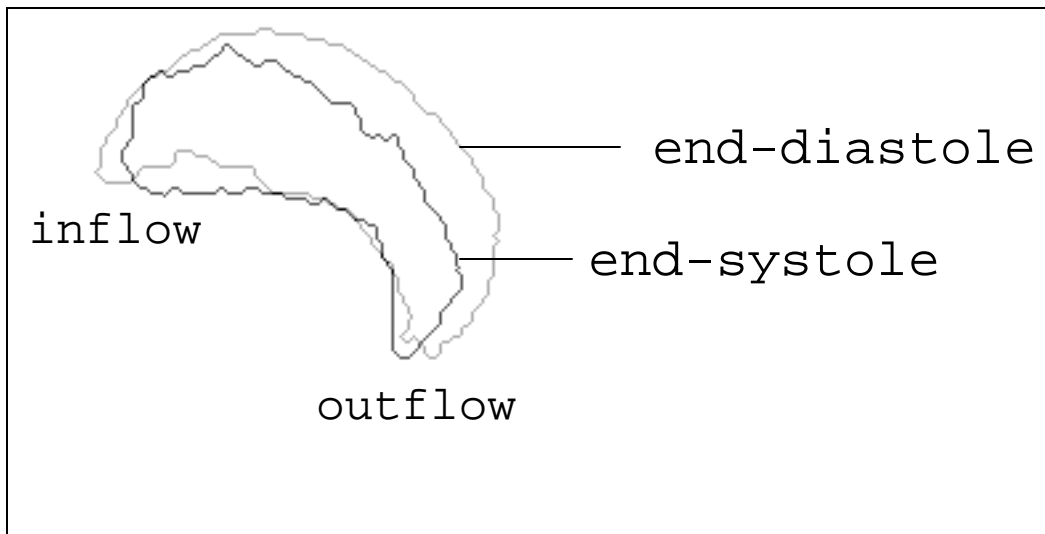


Figure 10. Short axis contours superimposed. No obvious difference due to twisting motion but clear asymmetry in contraction between inflow and outflow regions of freewall (convex portion of contour).

6. Conclusions

A pathwise formulation of the watershed has been found to be useful, particularly for characterizing the Meyer watershed and comparing it with alternate boundary formation techniques including the active contour and marker-driven gradient modification. Image anisotropy, which is a source of error in the surface reconstruction, can be objectively assessed in the RV image itself and then minimized by incorporation of the appropriate anisotropy in the sobel filter. Once the anisotropy has been thus minimized, application of the Meyer watershed to the 4D DSR image of the RV was found to be highly satisfactory providing precise information of subtle features of the dynamic RV shape. The diversity of the dynamic anatomy between the inflow and outflow regions of the RV supports the findings in an earlier 2D analysis of the passive heart^{16,17}.

7. References

1. J Sijbers, P Scheunders, M Verhoye, A Vander Linden, D Van Dyck, and E Raman. "Watershed-based segmentation of 3D MR data for volume quantization," *Magn Reson Imaging*, 15(6):679-688, 1997.
2. J Rogowska, K Batchelder, GSGazelle, EFHalpern, W Connor, and GLWolf. "Evaluation of selected two-dimensional segmentation techniques for computed tomographic quantization of lymph nodes," *Invest Radiol*, 31(3):138-145, 1996.
3. F Meyer and S Beucher. "Morphological Segmentation," *Journal of Visual Communication and Image Representation*, 1(1):21-46, 1990.
4. D Kim, "Multiresolutional Watershed Segmentation with User-Guided Grouping" *Proceedings of SPIE, Medical Imaging: Image Processing*, In Press (this volume)
5. WE Higgins and EJ Ojard. "Interactive morphological watershed analysis for 3D medical images," *Comput Med Imaging Graph*, 17(4/5):387-395, 1993
6. F Friedlander, "Le traitement morphologique d'images de cardiologie nucléaire," Doctoral thesis, School of Mines, Paris, Dec. 1989.
7. MC de Andrade, G Bertrand, and AA Ardaújo, "Segmentation of Microscopic images by flooding simulation: a catchment basins merging algorithm," *Proceedings of SPIE*, 3026:164-175, 1997.
8. JM Gauch and SM Pizer. "Multiresolution analysis of ridges and valleys in gray-scale images," *IEEE Transactions on Pattern Analysis and Machine Intelligence*. 15(6):635-646, 1993.
9. L Vincent and S Beucher. "The morphological approach to segmentation: an introduction," *Lecture notes for presentation at: Mathematische Morphologie und Digitale Bildverarbeitung, München*. Sept. 1989
10. LJ Sinak, EA Hoffman, and EL Ritman, "Subtraction gated computed tomography with the dynamic spatial reconstructor: simultaneous evaluation of left and right heart from single right-sided bolus contrast medium injection," *J Comput Assist Tomogr*, 8(1):1-9, 1984.
11. T Behrenbeck, JH Kinsey, LD Harris, RA Robb, and EL Ritman. "Three-dimensional spatial, density, and temporal resolution of the dynamic spatial reconstructor," *J Comput Assist Tomogr*, 6(6):1138-1147, 1982.
12. H Azhari, M Buchalter, S Sideman, E Shapiro, R Beyer. "A conical model to describe the non-uniformity of the LV twisting motion," *Ann Biomed Eng*, 20:149-165, 1992.
13. SM Jorgensen, SV Whitlock, PJ Thomas, RW Roessler and EL Ritman. "The dynamic spatial reconstructor: a high speed, stop action, 3-D, digital radiologic imager of moving internal organs and blood," *Proceedings of SPIE, Ultrahigh-and High-Speed Photography, Videography, Photonics, and Velocimetry*, 1346:180-191, 1990.
14. M Kass, A Witkin, and D Terzopoulos. "Snakes: active contour models," *Int. J. Comput. Vision* 1(4):321-331, 1988.
15. D Kucera and RW Martin. "Segmentation of sequences of echocardiographic images using a simplified 3D active contour model with region-based external forces," *Comput Med Imaging Graph*, 21(1):1-21, 1997.
16. PJ Yim, B Ha, CA Branch, GW Henry, TA Johnson and CL Lucas, "Thediastolic shape of the right ventricle of the heart," *Anat Rec*, in press (for March, 1998)
17. PJ Yim, B Ha, CA Branch, GW Henry, TA Johnson and CL Lucas, "Intuitive modeling of right ventricular shape," *Proc. SPIE; Medical Imaging 1997; Physiology and Function from Multidimensional Images*. 3033:373-382, 1997.
18. J Ferlinz, "Angiographic assessment of right ventricular volumes and ejection fraction," *Cathet Cardiovasc Diag*, 2(1):5-14, 1976
19. JS Rankin, PA McHale, CE Arentzen, D Ling, JC Greenfield, and RW Anderson, "The three-dimensional dynamic geometry of the left ventricle in the conscious dog," *Circ Res*, 39:304-313, 1976.

20. MP Feneley, JR Elbeery, JW Gaynor, SA Gall, JW Davis, and JW Rankin, "Ellipsoidal shell subtraction model of right ventricular volume," *Circ Res*, 67:1427-1436, 1990.
21. S Denslow, "An ellipsoidal shell model for volume estimation of the right ventricle from magnetic resonance images," *Academic Radiology*, 1(4):345-51, 1994
22. MD Parrish, TP Graham, ML Born, JP Jones, RJ Boucek, CL Partain, "Radionuclide ventriculography for assessment of absolute right and left ventricular volumes in children," *Circulation*, 66(4):811-9, 1982
23. MS Sacks, CJ Chuong, GH Templeton, and R Peshock, "In vivo 3-D reconstruction and geometric characterization of right ventricular free wall," *Ann Biomed Eng*, 21:263-276, 1993.
24. M Kuwahara, S Eiho, "3-D heart image reconstruction from MRI data," *Comput Med Imaging Graph*, 15:241-246, 1991.

Acknowledgements

We would like to sincerely thank Dr. Erik L. Ritman of the Department of Physiology and Biophysics at the Mayo Clinic for providing access to the DSR images and his assistant, Ms. Patricia E. Lund, for her technical help.